Materials Science & Engineering A 612 (2014) 236–245

Contents lists available at ScienceDirect

Materials Science & Engineering A

journal homepage: www.elsevier.com/locate/msea

Influence of welding parameter on mechanical properties and fracture behavior of friction stir welded Al–Mg–Sc joints

Y. Tao, Z. Zhang, D.R. Ni, D. Wang, B.L. Xiao, Z.Y. Ma *

Shenyang National Laboratory for Materials Science, Institute of Metal Research, Chinese Academy of Sciences, Shenyang 110016, China

ARTICLE INFO

Article history:
Received 17 September 2013
Received in revised form
18 May 2014
Accepted 14 June 2014
Available online 20 June 2014

Keywords:
Friction stir welding
Aluminum alloys
Microstructure
Mechanical properties
Fracture

ABSTRACT

8.1-mm thick Al–Mg–Sc plates were friction stir welded (FSW) at tool rotation rates of 400–800 rpm and welding speeds of 100–400 mm/min to investigate the effect of welding parameter on the microstructure, mechanical property and fracture behavior of joints. The lazy S and kissing bond, with quite different morphologies, were observed in the stir zone at 400 and 600 rpm, attributing to insufficient material flow. However, neither of them were detected at 800 rpm. Ultimate tensile strength of the joints was nearly equal to that of the base metal with the joint efficiency being 97–99%. Facture behavior of the joints changed with the welding parameter and it was strongly affected by the lazy S and kissing bond. For the joints at 400 and 600 rpm, fracture occurred partially along the lazy S at 100 mm/min or initiated at the kissing bond at 400 mm/min. However, the joints at 800 rpm exhibited a fracture independent of the lazy S or kissing bond. Furthermore, the present observations were compared with those made by other researchers and the reasons for insufficient material flow at lower rotation rates of 400 and 600 rpm were discussed.

1. Introduction

Friction stir welding (FSW), a solid-state joining technique invented by The Welding Institute of the United Kingdom in 1991, has been proven to be one of the most significant achievements in the field of joining aluminum alloys [1–3]. FSW offers several advantages, such as better mechanical properties, less distortion, and fewer welding defects as compared to conventional welding methods [1].

The material flow and weldability differed greatly when different aluminum alloys were welded by FSW. Peel et al. [4] reported that during FSW of 6082Al alloy, the material was more easily displaced, allowing the tool to settle into workpiece with less force as compared to 5083Al alloy. They attributed it to the fact that the flow stress of 6082Al alloy decreased more rapidly with the increase of temperature and thus a 6082Al weld would have a wider soft zone than a 5083Al one. In a study conducted by Fujii et al. [5], defect-free joints were obtained under almost all welding conditions used for 6061Al alloy whose deformation resistance was relatively low. However, the weldability was greatly affected by the rotation rate for 5083Al alloy whose deformation resistance was relatively high. It appears that intrinsic property of the aluminum alloys exerts a significant effect on the material flow in the FSW process.

In the stir zone (SZ) of FSW joints of Al–Mg based alloys such as 5083Al [6,7] as well as other aluminum alloys [8–10], a distorted faint line pattern, called the “zigzag line” or “lazy S”, was sometimes observed. It was indicated that the lazy S consisted of high density Al_2O_3 particles which originated from the oxide layer of the initial butt surface [8,11]. A continuous oxide film, often observed at the bottom of the SZ, was classified as the kissing bond by Sato et al. [12], which differed from the local and dense oxide particle distribution along the lazy S. Both the lazy S and kissing bond were prone to forming under low heat-input conditions [6,12], suggesting a lack of oxide layer disruption and insufficient material flow.

The addition of Sc to Al–Mg alloys gives rise to the precipitation of dispersive and nano-scaled coherent Al_3Sc particles. These particles imparted a significant strengthening effect and thus the ambient strength of Al–Mg–Sc alloys was improved significantly as compared to conventional Al–Mg based alloys [13]. Furthermore, Al_3Sc particles exhibited exceptional thermal stability [14–16], which would have two effects on the Al–Mg–Sc alloys. Firstly, Al_3Sc particles remained in the matrix below a certain temperature. A study of FSW Al–4.58Mg–0.26Sc (wt%) joint demonstrated that Al_3Sc particles were very stable against temperature increase during FSW [16]. They did not dissolve and showed no significant coarsening in the SZ compared to those in the base material (BM). Secondly, recrystallization was severely impeded by Al_3Sc particles

* Corresponding author. Tel./fax: +86 24 83978908.
E-mail address: zyma@imr.ac.cn (Z.Y. Ma).

http://dx.doi.org/10.1016/j.msea.2014.06.051
0921-5093/

[14,17], leading to an increase in recrystallization temperature and thus a narrower soft zone in the FSW temperature range.

Jones et al. [14] reported that cold rolled Al–0.25 wt% Sc alloy commenced recrystallization at ~500 °C. For a cold rolled 01570 (Al–5.76Mg–0.32Sc, wt%) alloy, subgrains remained stable at 350 °C even under dynamic condition (i.e., under stress) [17]. Zhao et al. [18] showed that broken fibrous tissues still existed in the SZ during FSW of 2-mm thick Al–Mg–Sc rolled plates. Both effects mentioned above would result in an increase in material deformation resistance and be unfavorable for material flow in the FSW process. So the weld processing window and specific microstructure that might appear during FSW of Al–Mg–Sc alloys are worth in-depth investigation.

Unfortunately, FSW investigations of Al–Mg–Sc alloys have been limited so far [16,18,19]. On one hand, very few studies on FSW of Al–Mg–Sc alloys were conducted under a single welding parameter [19], or even without providing welding parameter and tool geometry [18]. Investigation on the effect of welding parameter on the microstructure and mechanical properties of FSW Al–Mg–Sc joints is lacking. On the other hand, for Al–Mg–Sc alloys with relatively high deformation resistance, the specific microstructure which might appear in the SZ due to reduced material flow during FSW remained unknown. Instead, a previous study on FSW of Al–Mg–Sc alloy by Sauvage et al. [16] focused on the variation of Al_3Sc particle distribution in the SZ as compared to the BM. Besides, it was reported that variation of welding parameter could result in the change in the shape of lazy S [10]. However, systematical studies on how those changes in the shape and structure of lazy S with welding parameter could affect the fracture behavior of FSW joints have not been reported.

In the present study, an Al–Mg–Sc alloy was subjected to FSW under a wide range of welding parameters. A specific microstructure containing both the lazy S and kissing bond was observed on the cross-section of the SZ. The effect of welding parameter on the variations of microstructure in the SZ, such as shape and structure of lazy S and kissing bond and how those variations affect the mechanical property and fracture behavior of joints were deeply analyzed.

2. Experimental

8.1-mm thick as-extruded Al–5.33Mg–0.23Sc–0.49Mn–0.14Fe–0.06Zr (wt%) plate was used in this study. FSW was carried out along the extrusion direction at tool rotation rates of 400, 600, and 800 rpm and travel speeds of 100 and 400 mm/min. A welding tool with a concave shoulder 20 mm in diameter, and a threaded cone-shaped pin 8 mm in root diameter and 7.8 mm in length was used. The plunge depth of the shoulder was controlled at ~0.25 mm. The top and butt surfaces of all the plates were cleared with abrasive papers, and then cleaned with alcohol prior to welding.

The specimens for microstructural examination were cross-sectioned perpendicular to the FSW direction, polished, and then aged at 120 °C for 16 h to emphasize the grain boundaries. These specimens were soaked in a 2 g NaOH + 100 ml H_2O aqueous solution for 20 min and then washed with 20% nitric acid and alcohol solution. The microstructure was examined using optical microscopy (OM) and scanning electron microscopy (SEM, Quanta600). The precipitates in various zones on the cross-section of the welds were examined using transmission electron microscopy (TEM, TECNAI 20). Thin foils for TEM were prepared by twin jet-polishing using a solution of 30% methanol and 70% nitric acid at −30 °C and 13 V.

Hardness measurement was conducted on the transverse cross-section of the welds along the mid-thickness of the plate using an automatic testing machine (Leco, LM-247AT) under a load of 500 g for 15 s. The tensile specimens with a gauge length of 40 mm and a width of 10 mm were machined perpendicular to the FSW direction. Subsized tensile specimens with a gauge length of 23 mm and a width of 4 mm were employed for the BM. Room-temperature tensile tests were carried out at a constant strain rate of $1 \times 10^{-3}\ s^{-1}$, and the property data for each condition was obtained by averaging the three test results. The fracture surfaces of tensile specimens were examined using SEM.

3. Results

3.1. Microstructure

Cross-sectional macrographs of FSW Al–Mg–Sc joints under different welding parameters are presented in Fig. 1. Sound welds were achieved under a rotation rate range of 400–800 rpm and a traverse speed range of 100–400 mm/min. It is interesting to note that for the joints at lower rotation rates of 400 and 600 rpm, inhomogeneous macrostructures were observed in the SZ (Fig. 1(a)–(d)). A dominating feature of the macrostructure was the partially developed banded structure, which was located mainly in the advancing side (AS) and extending toward the retreating side (RS). Optical micrographs of the banded region are presented in Fig. 2. It was revealed that alternating dark and white bands corresponded to local fine grain zones and coarse grain zones, respectively. As shown in Fig. 1, increasing the rotation rate or decreasing the traverse speed led to the transformation of the banded structure to onion rings. At 800 rpm and 100 mm/min, a homogeneous macrostructure consisting of well developed onion rings was now generated in the SZ (Fig. 1(e)). The average grain size of the SZ, determined by the mean linear intercept technique, was only slightly increased by either increasing the rotation rate or decreasing the traverse speed (Table 1).

Lazy S was distinctly visible at rotation rates of 400 and 600 rpm (Fig. 1(a)–(d)), while it could hardly be detected at 800 rpm (Fig. 1(e) and (f)). Fig. 3 shows the microstructure of the lazy S under both OM and SEM. A curve line with white contrast was clearly distinguished at lower magnification by OM (Fig. 3(a)). The white contrast of the curve line was caused by different etching responses between a relatively coarser grain zone with a width of ~5 μm and ambient finer grains (Fig. 3(b)). Closer observation revealed that local and dense micro-cavities were distributed discontinuously along the lazy S (Fig. 3(c)). EDS analyses (Fig. 3(d)) on the particles in the micro-cavity region revealed a high oxygen content (23 at%), which is similar to the results obtained in FSW 7075Al-T651 alloy by Ren et al. [11]. It appeared that these micro-cavities resulted from exfoliation of oxide particles, which originated from the oxide layer of initial butt surface, from the specimen surface during etching [8,12].

A continuous curve line was also observed at the bottom of the SZ at rotation rates of 400 and 600 rpm (Fig. 4(a)), in addition to the lazy S appearing in the middle and upper parts of the SZ. The continuous dark line consisted of huge amounts of micro-voids at higher magnification under OM (Fig. 4(b)). Those micro-voids gathered together linking up to a continuous ravine in the appearance of a crack under SEM (Fig. 4(c)). These crack-like appearances also resulted from the detachment of numerous fine oxide particles from the specimen during etching [12]. This result indicated that a continuous oxide film developed at the root tip of the SZ, which was defined as the “kissing bond” [12].

The length of the kissing bond changed with the welding parameter. Increasing the traverse speed led to the formation of a longer kissing bond. Under rotation rates of 400 and 600 rpm for a constant traverse speed of 100 mm/min, a kissing bond about 300 μm in length was detected, while as the traverse speed reached

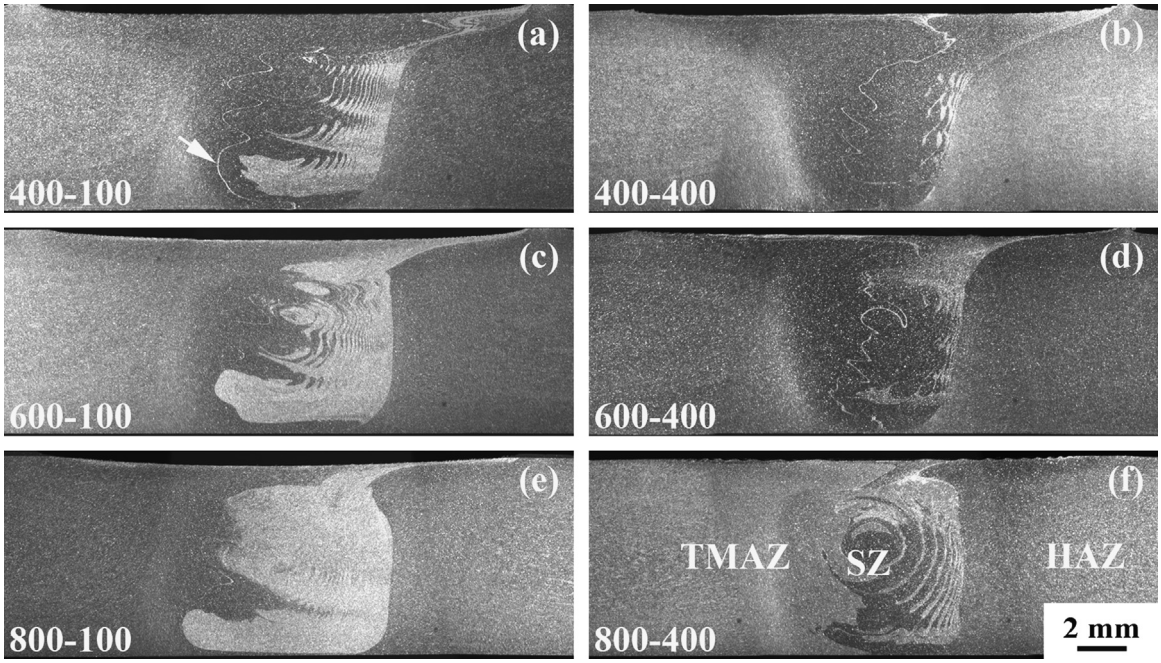

Fig. 1. Cross-sectional macrographs of FSW Al–Mg–Sc joints under different welding parameters (rpm–mm/min, the advancing side is on the right).

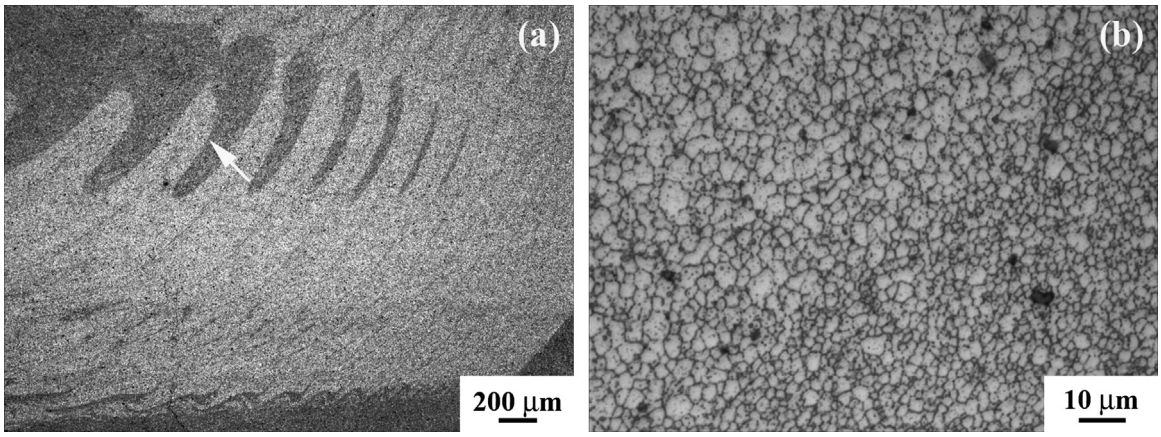

Fig. 2. (a) Optical microstructure of banded region in Fig. 1(a), and (b) higher magnification image of the band interface as indicated by the arrow in (a).

Table 1
Average grain size of the SZs under various welding parameters (μm).

Rotation rate (rpm)	Traverse speed (mm/min)	
	100	400
400	5.7	4.9
600	6.7	5.9
800	7.8	6.1

400 mm/min, a kissing bond about 600 μm in length was observed. No kissing bonds were found at 800 rpm.

Optical micrographs of four typical zones on the cross-section of the weld at 400 rpm and 100 mm/min are shown in Fig. 5. The microstructure in the transition zone between SZ and thermal mechanically affected zone (TMAZ) was composed of two parts (Fig. 5(a)). The left part corresponded to equiaxed grains in the SZ. Elongated grains, surrounded by equiaxed ones, appeared in the TMAZ bordering the SZ on the right part. As the distance from the weld center increased, elongated grains were distributed along the upward streamlines in the middle of the TMAZ (Fig. 5(b)). Pancake-like grains arranged along the extrusion direction were detected both in the heat affected zone (HAZ) and the BM. The microstructure in the two regions did not reveal apparent difference (Fig. 5(c) and (d)).

As shown in TEM bright field image in Fig. 6(a), fine Al_3Sc particles with coherent strain contrast were distributed uniformly in the BM. The selected area electron diffraction (SAED) pattern taken in a ⟨001⟩ Al zone axis clearly showed the superlattice reflections of Al_3Sc particles (Fig. 6(b)), which further confirmed the coherence of those particles with the matrix. Similar phenomena were also observed in the HAZ (Fig. 6(c)) and in the SZ/TMAZ (Fig. 6(d)), with the size of coherent Al_3Sc particles being almost unchanged. No significant coarsening of Al_3Sc particles was observed in the SZ and the size of most particles was less than 20 nm (Fig. 6(e)). This indicated that Al_3Sc particles were resistant to coarsening during the FSW process. Generally, Al_3Sc particles in the SZ were still coherent with the matrix, based on the results from the SAED pattern (not shown here). However, some large-sized Al_3Sc particles lost their coherence with the matrix (Fig. 6(e)), which explained the faint superlattice reflections as indicated by the white circle in Fig. 6(f).

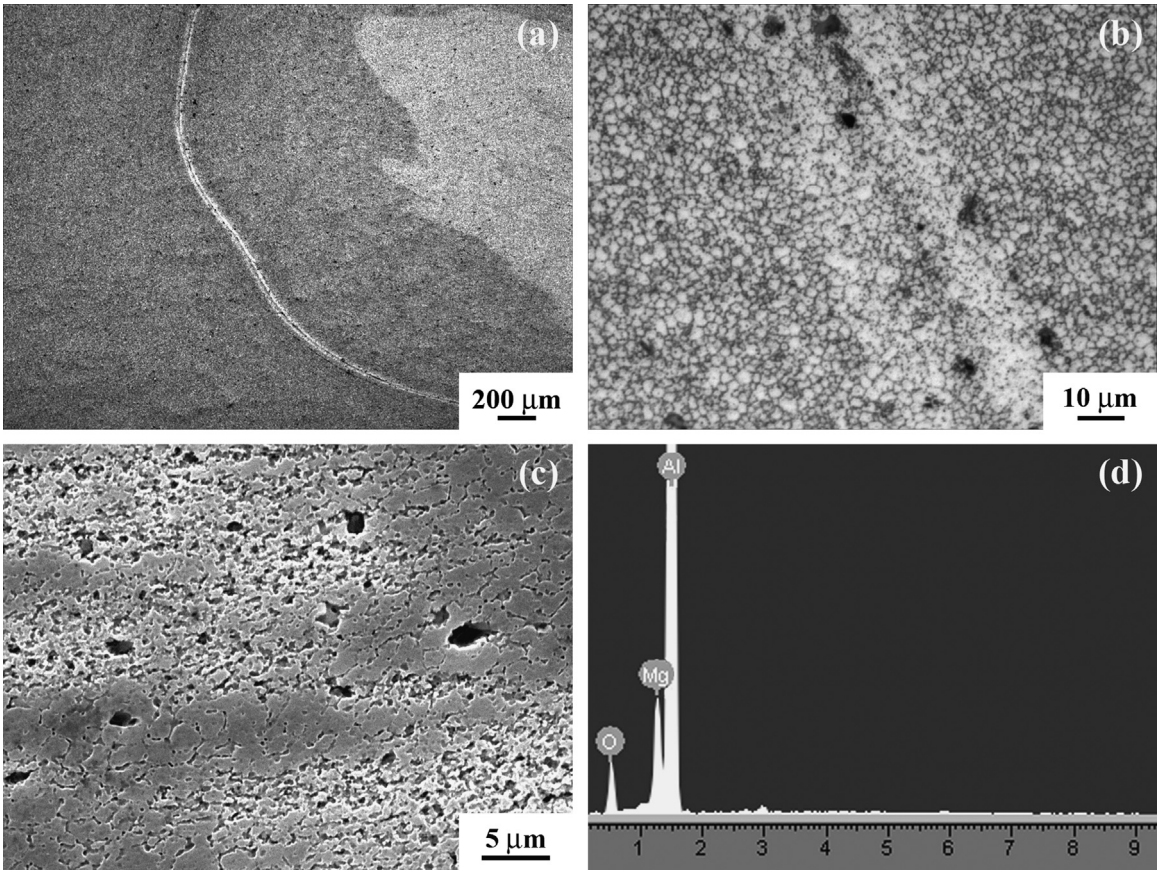

Fig. 3. Microstructure of the lazy S in the arrow region in Fig. 1(a) (400 rpm and 100 mm/min): (a) lower and (b) higher magnification images under OM, (c) image under SEM, and (d) EDS spectrum of the particles in micro-cavity region in (c).

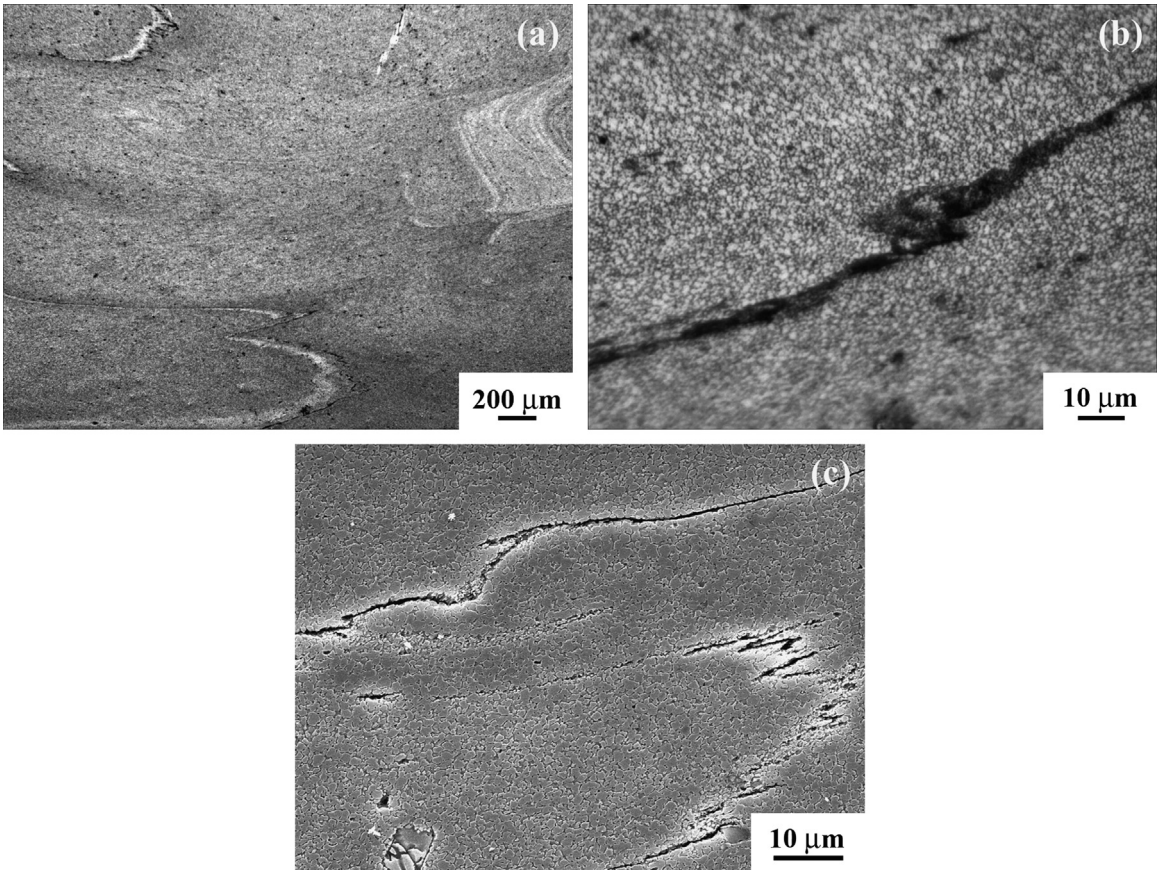

Fig. 4. Microstructure of the kissing bond at the root tip of the SZ (400 rpm and 400 mm/min): (a) lower and (b) higher magnification images under OM, and (c) image under SEM.

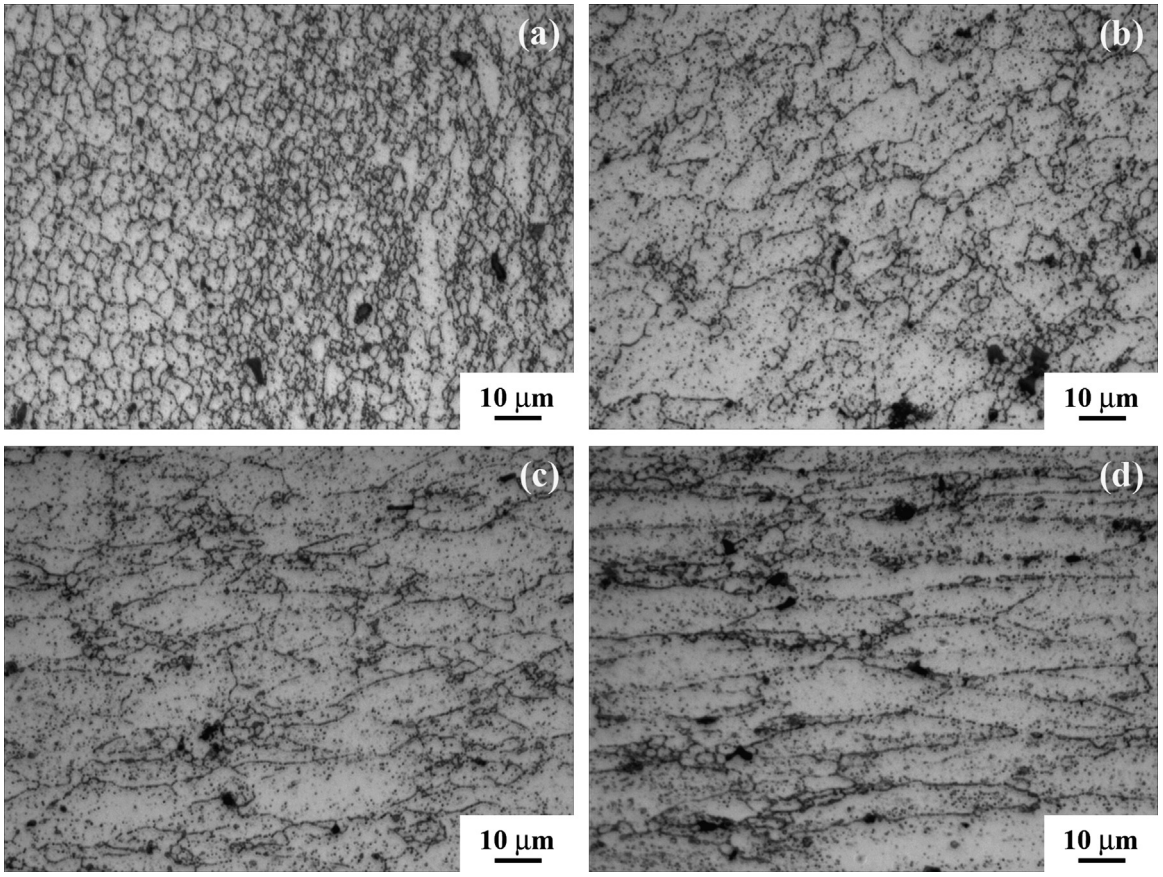

Fig. 5. Optical microstructures of various zones on the cross-section of FSW Al–Mg–Sc joint (400 rpm and 100 mm/min): (a) SZ/TMAZ on AS, (b) TMAZ, (c) HAZ, and (d) BM.

3.2. Hardness profile

The Vickers hardness profiles measured on the cross-sections of the joints along the mid-thickness of the plates are shown in Fig. 7. It is noted that the hardness distribution across the weld from the BM to the SZ was roughly homogeneous for various welds, with the discrepancy between maximum and minimum values being less than 10 Hv. Besides, the change in the welding parameter did not exert a significant influence on the hardness profiles, although the hardness values of the SZ did slightly decrease as the rotation rate increased from 400 to 800 rpm. Previous research suggested that hardness profile of FSW aluminum alloy joints depended greatly on the precipitate distribution and only slightly on the grain size [20]. Thus the roughly homogeneous hardness profiles could have an intimate relationship with the good thermal stability of Al_3Sc particles during FSW (Fig. 6).

3.3. Tensile property and fracture behavior

Transverse tensile properties of FSW Al–Mg–Sc joints are summarized in Table 2. It was found that ultimate tensile strengths (UTS) of the joints were nearly equal to those of the BM with the joint efficiency being 97–99%, and they were insensitive to changes in the welding parameter. However, the fracture behavior of the joints varied with the welding parameter and was strongly affected by the lazy S and kissing bond. For the joints at lower rotation rates of 400 and 600 rpm, fracture was revealed to be partially along the lazy S at 100 mm/min or to initiate at the kissing bond at the root tip of the SZ at 400 mm/min. However, the joint at a higher rotation rate of 800 rpm exhibited 45° shear fracture in the SZ without preferential crack initiation source, which was independent of the lazy S or kissing bond. Examples of the three typical types of failed FSW Al–Mg–Sc joints are given in Fig. 8.

It was interesting to note that apart from failure at the lazy S or kissing bond, 45° shear fracture along the boundary between the SZ and TMAZ was also revealed in the joints at 400 and 600 rpm. An example of such a failed joint is given in Fig. 9. By comparing the tensile property of joints with the above two failure locations (Table 3), it was found that neither the lazy S nor the kissing bond exerted a significant effect on the tensile strength of FSW Al–Mg–Sc joints, although the elongation was considerably reduced.

Typical SEM fractographs of the joint failed partially along the lazy S are presented in Fig. 10. The fracture surface exhibited a fluctuated appearance (Fig. 10(a)). The region failed along the lazy S (point B) was characterized by very fine micro-voids (Fig. 10(b)), indicating significantly reduced ductility. However, most of the other regions with the fracture path away from the lazy S exhibited a larger equiaxed dimple morphology (Fig. 10(c) and (d)), indicating extensive plastic deformation. Fig. 11(a) shows typical SEM fractograph of the joint with the crack initiated at the kissing bond. No large dimples or tearing ridges were observed at the bottom corresponding to the location of the kissing bond (Fig. 11(b)), suggesting relatively low plasticity in that area. Besides, micro-cracks were clearly observed to form initially in that region (Fig. 11(b)). However, larger dimples and tearing ridges were revealed in most of the other fracture surfaces (Fig. 11(c)).

4. Discussion

4.1. Influence of welding parameter on macrostructure

For the joints at lower rotation rates of 400 and 600 rpm, macrostructures in the SZ were inhomogeneous and contained

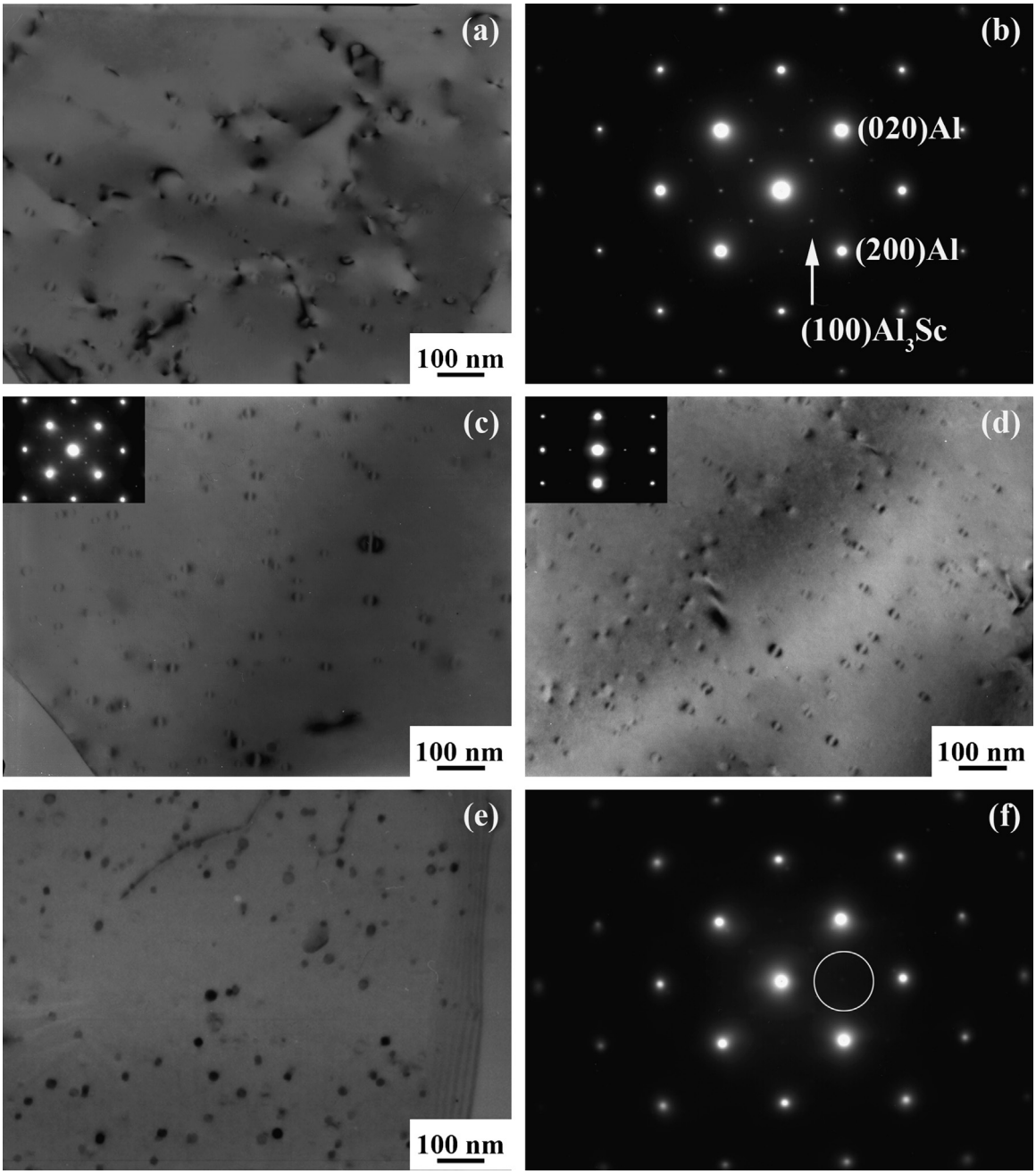

Fig. 6. (a) TEM bright field image of BM and (b) corresponding SAED pattern of ⟨001⟩ zone axis, (c) and (d) bright field images of the HAZ and SZ/TMAZ, respectively (the insets correspond to SAED patterns of ⟨001⟩ and ⟨112⟩ zone axes, respectively), (e) bright field image of the SZ and (f) corresponding SAED pattern of ⟨001⟩ zone axis (400 rpm and 100 mm/min).

partially developed banded structure (Fig. 1(a)–(d)). The bands were revealed to be different in grain size (Fig. 2). The present observation was consistent with that in friction stir processed as-cast 7075Al alloy by Liu et al. [21]. They suggested that the banded structure was formed as a result of insufficient material flow when a low rotation rate was used. Thus deformation extent varied in local regions of the SZ. However, at a higher rotation rate of 800 rpm at 100 mm/min, a homogeneous macrostructure consisting of well developed onion rings was observed in the SZ (Fig. 1(e)). It was due to the fact that a higher rotation rate intensified the frictional heating and the stirring effect and subsequently more sufficient flow of the material occurred in the SZ.

Lazy S was distinctly visible at rotation rates of 400 and 600 rpm (Fig. 1(a)–(d)), while it could hardly be detected at 800 rpm (Fig. 1(e) and (f)). It is well documented that lazy S consisted of high density Al_2O_3 particles which originated from the initial butt surface oxide layer [8,11]. The oxide layer was broken up during FSW under the stirring of the pin, and the broken pieces flowed collectively along with the mixing of the material [8]. Relatively weak stirring at 400 and 600 rpm resulted in inadequate scattering of the broken products. Thus local and dense oxide particles were distributed discontinuously along the flow path of the initial butt surface, forming the lazy S (Fig. 3). Increasing the rotation rate to 800 rpm produced more intensive stirring of the material, which allowed full dispersion of the broken products in the SZ during FSW. Thus lazy S was hardly observed at 800 rpm (Fig. 1(e) and (f)).

In addition to the lazy S appearing in the middle and upper parts of the SZ, the kissing bond was observed at the bottom at 400 and 600 rpm (Fig. 4(a)). It is noted that fine equiaxed grains

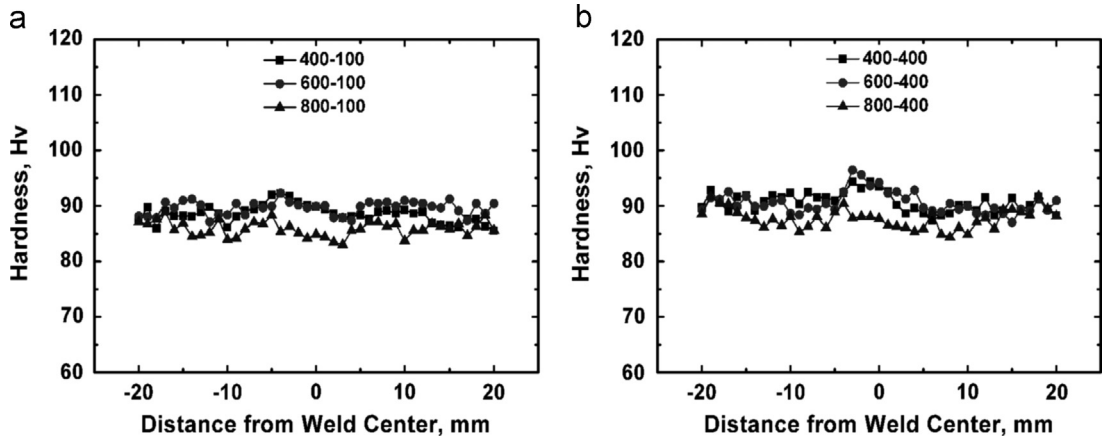

Fig. 7. The Vickers hardness profiles of FSW Al–Mg–Sc joints under different welding parameters (rpm–mm/min, the AS is on the right).

Table 2
Transverse tensile property of FSW Al–Mg–Sc joints.

Weld parameter (rpm–mm/min)	YS (MPa)	UTS (MPa)	Weld efficiency (%)	Failure location
BM	245 ± 3.5	368 ± 1.0		
400–100	226 ± 0.9	365 ± 2.1	99.4	Lazy S, TMAZ/SZ
400–400	231 ± 3.4	360 ± 7.4	98.0	Kissing bond, TMAZ/SZ
600–100	213 ± 2.4	364 ± 4.6	99.0	Lazy S, TMAZ/SZ
600–400	224 ± 6.0	356 ± 8.8	97.0	Kissing bond, TMAZ/SZ
800–100	198 ± 0.7	357 ± 2.1	97.0	SZ
800–400	226 ± 0.9	363 ± 4.1	98.7	SZ

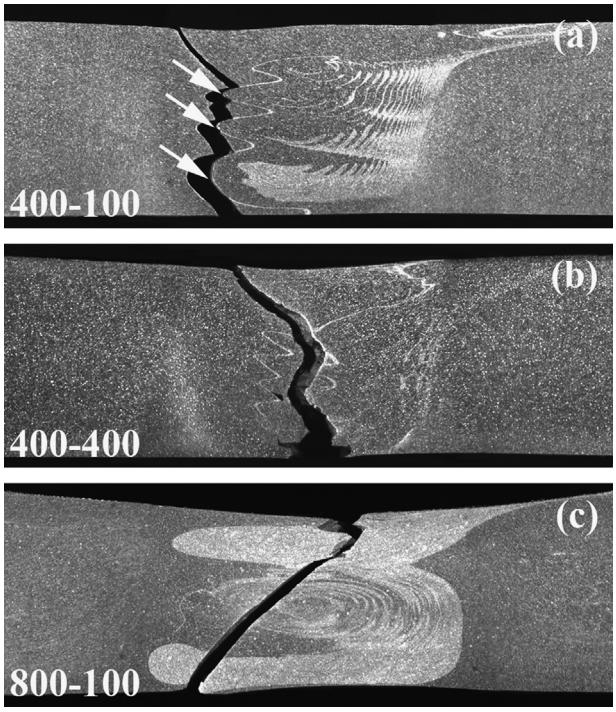

Fig. 8. Three typical types of failed FSW Al–Mg–Sc joints (rpm–mm/min): (a) fracture was partially along the lazy S, (b) fracture initiated at the kissing bond at the root tip of the SZ and (c) 45° shear fracture in the SZ.

rather than pancake extruded microstructure of the BM were observed around the kissing bond and also at the lower part of the SZ (Fig. 4(b)), suggesting that in these areas the material underwent stirring and consequent deformation to an extent, and as a result complete dynamic recrystallization took place. Thus the kissing bond is likely to be related to a low-heat input welding condition rather than insufficient plunging of the welding tool, because no unwelded butt surface remained at the root side. Compared to the middle and upper parts of the SZ, the stirring effect of the pin was significantly weakened in the lower part. Hence the oxide layer deriving from the initial butt surface suffered inadequate disruption, and as a result a continuous oxide film was formed at the root tip of the SZ, namely, the kissing bond. Under lower rotation rates of 400 and 600 rpm, an increase in the traverse speed from 100 to 400 mm/min further weakened the stirring of material per unit advance of the tool, and thus led to the formation of a longer kissing bond.

To provide a deep understanding of the macrostructure in the SZ, the change of the lazy S with the welding parameter was correlated with the variation of the banded structure. At a welding speed of 100 mm/min, for a lower rotation rate of 400 rpm, both partially developed banded structure and lazy S were observed; however, at a higher rotation rate of 800 rpm, while the onion rings developed, the lazy S almost disappeared. This result is in good agreement with that in FSW 6061Al-T6 alloy by Xu et al. [10]. They reported that lower rotation rate did not result in mixing of materials from the advancing side and the retreating side. However, at a higher rotation rate, the retreating side material was caught between layers of the advancing side material, forming the

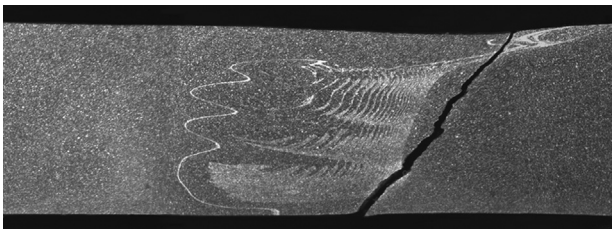

Fig. 9. Failed FSW Al–Mg–Sc joints showing 45° shear fracture in the SZ/TMAZ on the AS (400 rpm and 100 mm/min).

Table 3
Tensile property comparison between joints at the same weld parameter but with different fracture features.

Weld parameter (rpm–mm/min)	YS (MPa)	UTS (MPa)	EL (%)	Failure location
400–100	227	367	21.7	Lazy S
	226	364	26.5	TMAZ/SZ
400–400	233	355	17.8	Kissing bond
	228	366	22.9	TMAZ/SZ

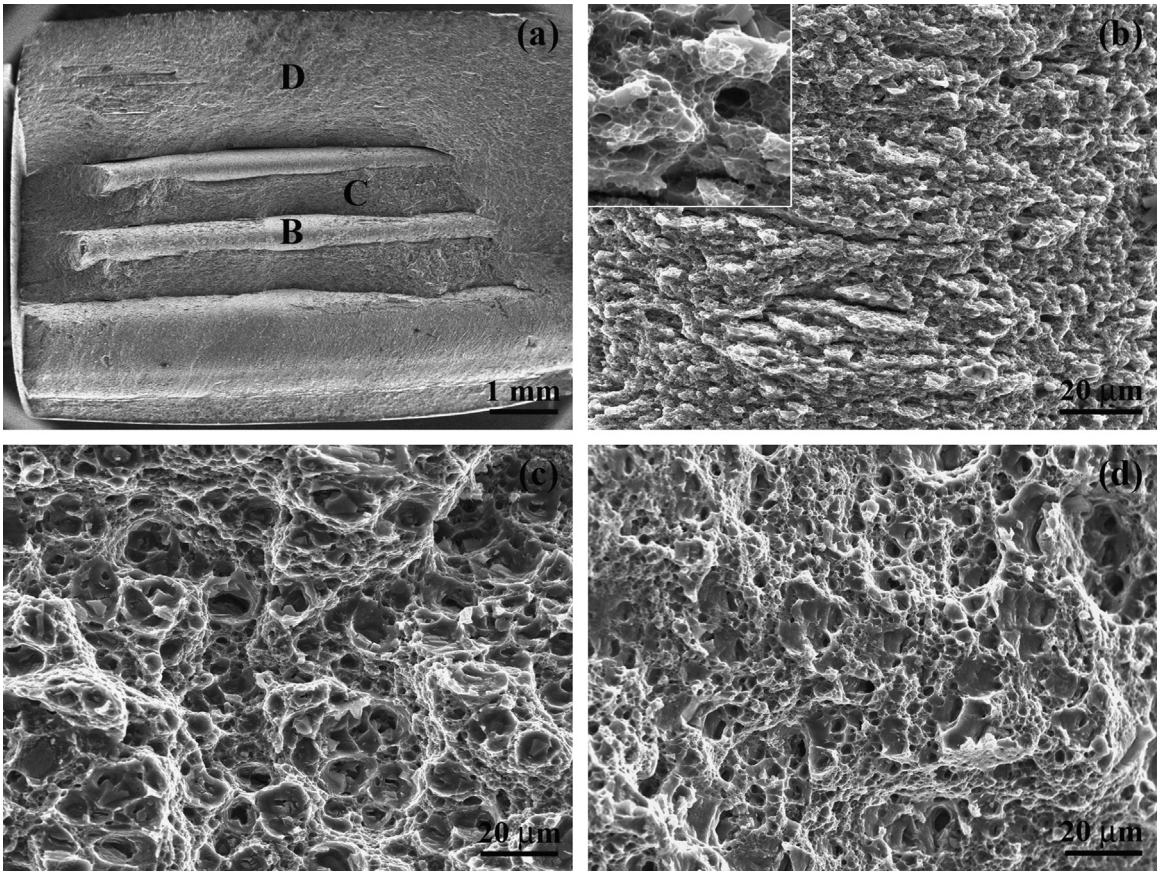

Fig. 10. SEM fractographs of the joint failed partially along the lazy S (400 rpm and 100 mm/min): (a) macroscopic view, (b)–(d) regions corresponding to B, C and D in (a).

onion rings. Thus mixing of materials from the two sides was generated. Besides, the oxide layer on the initial butt surface was dragged into the onion ring region and mixed with the ring. Thus the lazy S could not be identified. To sum up, variation of macrostructure in the SZ with the welding parameter essentially reflected change of the material mixing state. As the rotation rate increased, the mixing extent of materials from the two sides increased, which was also consistent with the results in FSW joints of dissimilar aluminum alloys [4,22].

4.2. Influence of welding parameter on fracture behavior

In a study on FSW joints of dissimilar aluminum alloys, obvious lazy S between two alloys, indicating a lack of mixing, was revealed in the SZ when a lower rotation rate was used [22]. However, the welds failed in the lowest hardness zone in the HAZ rather than along the lazy S, suggesting that the lazy S did not influence the failure location of welds when an obvious lowest hardness zone was generated. However, a low hardness plateau extending more than 15 mm from the weld center was observed on hardness profile of FSW 5083Al joint [6]. Besides, the lazy S appeared to be obvious and continuous at a higher traverse speed. In this case, the fracture occurred along the lazy S for FSW 5083Al joints. It can be speculated that whether the lazy S had an effect on the fracture feature of FSW joints depended on two prerequisites. One was a continuous lazy S with very low extent of disruption. The other was a roughly homogeneous hardness profile, i.e., no obvious lowest hardness zone was observed. Only if both conditions were satisfied did the fracture at the lazy S may occur during tension.

During FSW of Al–Mg–Sc alloy, relatively homogeneous hardness profiles were achieved (Fig. 7). In this case, the fracture behavior of the joints changed with the welding parameter and it was strongly affected by the lazy S and kissing bond. At lower rotation rates of 400 and 600 rpm, the oxide array was either in the form of local and dense particle distribution along the lazy S (Fig. 3) or continuous oxide film at the root tip of the SZ, i.e., kissing bond (Fig. 4). These oxide-rich regions would be directly bonded by oxide particles, indicating poor local bonding strength. These regions tended to become crack initiation sources and exhibited poor ductility during tension (Figs. 10(b) and 11(b)). Therefore, for the joints at 400 and 600 rpm, fracture occurred partially along the lazy S at 100 mm/min or initiated at the kissing bond at the root tip of the SZ at 400 mm/min (Fig. 8(a) and (b)). The change of crack initiation site at 400 mm/min could be due to the development of a longer and more conspicuous kissing bond as the traverse speed increased. However, at a higher rotation rate of 800 rpm, a good mixture of the advancing side and retreating side materials was generated, with metallic bond being completely achieved in the whole SZ. Therefore, the joint at 800 rpm exhibited a fracture independent of the lazy S and kissing bond (Fig. 8(c)).

Apart from failure at the lazy S or kissing bond, 45° shear fracture along the boundary between the SZ and TMAZ was also revealed in the joints at 400 and 600 rpm (Fig. 9). During the tensile test of FSW joints, the fracture at the SZ/TMAZ boundary was reported in previous studies [23–25] and several explanations were proposed. Lim et al. [23] reported that for AZ31B-H24 Mg alloy joints, crack initiated at a certain region with high oxygen content between the TMAZ and SZ. This was attributed to accumulation of broken oxide products at a particular location where plastic flow did not occur. Liu et al. [25] pointed out that the tensile fracture of FSW 2017Al alloy joints at or near the SZ/TMAZ boundary was attributed to the remarkable difference in the microstructures between the TMAZ and SZ, which was also observed in the present

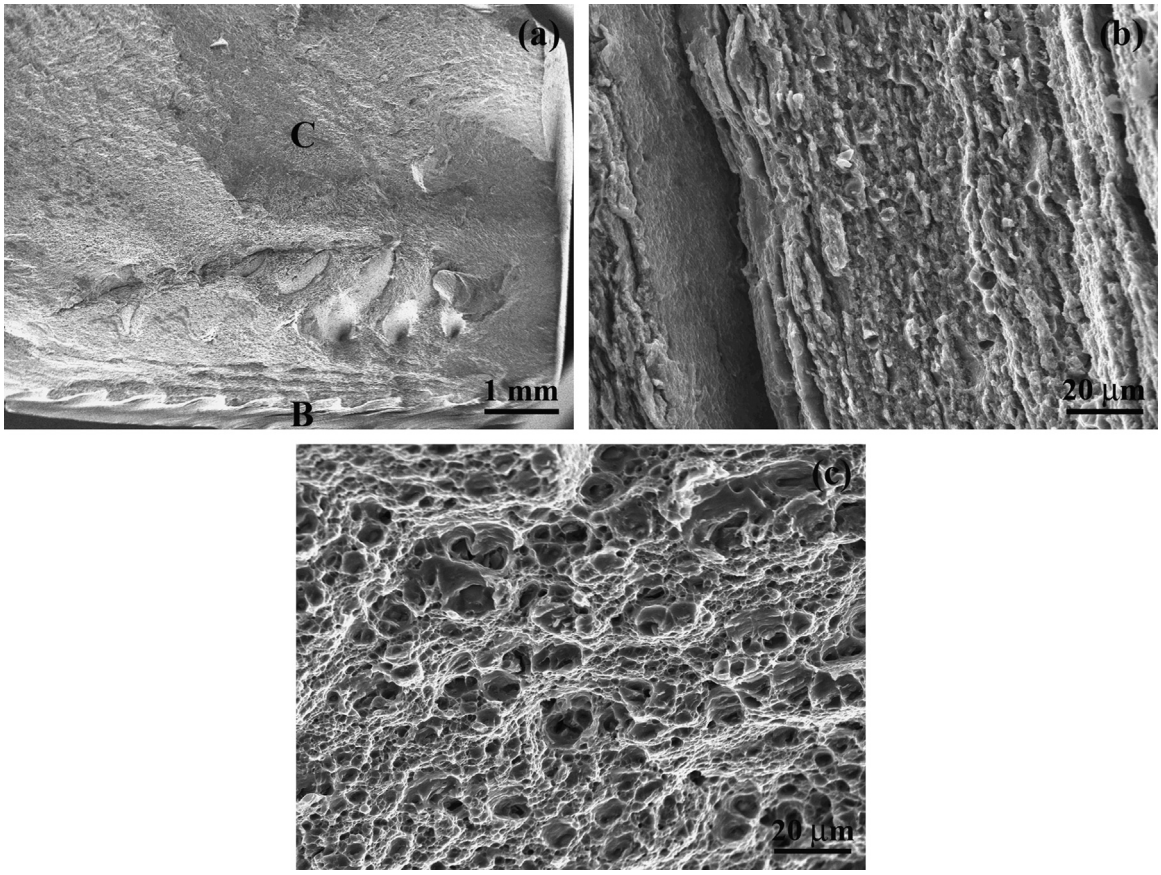

Fig. 11. SEM fractographs of the joint with the crack initiated at the kissing bond at the root tip of the SZ (400 rpm and 400 mm/min): (a) macroscopic view, (b) and (c) regions corresponding to B and C in (a).

study (Fig. 5(a) and (b)). However, Sato et al. [26] suggested that for a joint having a homogeneous hardness profile, fracture location depended on both crystallographic-orientation distribution of the matrix grains and strain tensor of the imposed deformation.

For the present Al–Mg–Sc joints with roughly homogeneous hardness distribution, it appeared that reasons for the fracture along the SZ/TMAZ boundary were complicated and needed in-depth investigation. Comparison of tensile properties between the joints failed at the lazy S or kissing bond and those failed at the SZ/TMAZ boundary indicated that neither the lazy S nor kissing bond exerted a significant effect on the tensile strength of the joints (Table 3). In the meanwhile, hardness profiles of the joints were relatively homogeneous and insensitive to welding parameter. In this case, little variation in UTS was expected for the present FSW Al–Mg–Sc joints (Table 2). This was presumably due to the fact that metallurgical bonding was completely achieved between the oxide-free surfaces along the lazy S. This differed from the results by Peel et al. [6], who found that the FSW 5083Al joints welded at higher traverse speed cracked along the lazy S and exhibited much lower UTS as compared to those welded at lower traverse speed.

4.3. Material flowabitity during FSW of 8.1-mm thick Al–Mg–Sc plate

As mentioned above, the intrinsic property of the aluminum alloys exerts a significant effect on the material flow in the FSW process [4,5]. During FSW of 8-mm thick 7075Al-T651 plates, Ren et al. [11] employed a tool with the same size and shape as that in the present study. They reported that the onion rings were well developed and no trace of the lazy S was observed at 600 rpm and 100 mm/min, indicating good material mixing. However, in this study, both partially developed banded structure and faint lazy S were detected under the same parameter. This implies that the extent of material mixing differed greatly when different aluminum alloys were used during FSW. As mentioned above, Al_3Sc particles had exceptional thermal stability [14–16]. They remained in the matrix below a certain temperature and inhibited the material flow. Besides, they severely impeded recrystallization, resulting in a narrower soft zone in the FSW temperature range [17,18]. Thus an increase in material deformation resistance and a reduced material flow were expected during FSW of Al–Mg–Sc alloy. As a result, at 600 rpm and 100 mm/min, FSW did induce thorough material mixing and complete oxide layer disruption for 7075Al alloy [11]. However, that was not the case for the Al–Mg–Sc alloy in this study.

Material flow during the FSW process was also affected by the thickness of the welded plate. During FSW of ZK60 Mg alloy by Mironov et al. [27], defect-free welds were produced for 3-mm thick plates, whereas 6-mm thick welds were defective irrespective of the welding parameter used. They suggested that the formation of defects was associated with insufficient material flow since the maximum temperature reached in the thicker plates was lower than that in the thinner ones.

In general, material flow during FSW depended on several factors, such as welding parameters, intrinsic property of materials, thickness of welding plate, as well as shape and size of the welding tool [5,6]. For the 8.1-mm thick Al–Mg–Sc plates whose deformation resistance is relatively high, partially developed banded structure as well as the lazy S and kissing bond was obtained at lower rotation rates of 400 and 600 rpm (Fig. 1(a)–(d)), suggesting a lack of material mixing and oxide layer disruption. However, at a higher rotation rate of 800 rpm at 100 mm/min,

the onion rings were well developed and the lazy S disappeared, indicating a good mixture between the advancing side and retreating side materials. Thus for a material with high deformation resistance in the FSW temperature range, such as Al–Mg–Sc, the low rotation rate and high traverse speed were clearly not suitable for the FSW process. An appropriate hot welding condition is desired.

5. Conclusions

1. At lower rotation rates of 400 and 600 rpm, a partially developed banded structure was observed in the SZ. Increasing the rotation rate led to the transformation of the banded structure to the onion rings. At a higher rotation rate of 800 rpm at 100 mm/min, well developed onion rings were generated in the SZ.
2. The lazy S and kissing bond, with quite different morphologies, were observed in the SZ at 400 and 600 rpm. However, neither of them was visible at 800 rpm. Local and dense oxide particles were distributed discontinuously along the lazy S; while a continuous oxide film was detected at the root tip of the SZ, forming the kissing bond. Increasing the traverse speed from 100 to 400 mm/min gave rise to a longer kissing bond.
3. Hardness distribution from the BM to the SZ was roughly homogeneous for various joints. Ultimate tensile strength of the joints was nearly equal to that of the BM with the joint efficiency being 97–99%.
4. Facture behavior of the joints changed with the welding parameter and it was strongly affected by the lazy S and kissing bond. For the joints at 400 and 600 rpm, fracture was revealed to be partially along the lazy S at 100 mm/min or to initiate at the kissing bond at 400 mm/min. However, the joints at 800 rpm exhibited a fracture independent of the lazy S or kissing bond.
5. For 8.1-mm thick plates of Al–Mg–Sc alloy whose deformation resistance is relatively high, FSW did not result in sufficient material flow in the SZ at lower rotation rates of 400 and 600 rpm. However, thorough material mixing and complete oxide layer disruption were produced at 800 rpm and 100 mm/min. Thus for Al–Mg–Sc alloy with high deformation resistance in the FSW temperature range, an appropriate hot welding condition is needed.

Acknowledgments

This work was supported by the National Natural Science Foundation of China under Grant no. 51331008.

References

[1] R.S. Mishra, Z.Y. Ma, Mater. Sci. Eng. R 50 (2005) 1–78.
[2] E.D. Nicholas, W.M. Thomas, Int. J. Mater. Prod. Technol. 13 (1998) 45–55.
[3] W.M. Thomas, E.D. Nicholas, J.C. Needham, P. Temple-Smith, S.W.K.W. Kallee, C.J. Dawes, Friction Stir Butt Welding, International Patent Application no. GB2306366-A, May 1997.
[4] M.J. Peel, A. Steuwer, P.J. Withers, T. Dickerson, Q. Shi, H. Shercliff, Metall. Mater. Trans. A 37 (2006) 2183–2193.
[5] H. Fujii, L. Cui, M. Maeda, K. Nogi, Mater. Sci. Eng. A. 419 (2006) 25–31.
[6] M. Peel, A. Steuwer, M. Preuss, P.J. Withers, Acta Mater. 51 (2003) 4791–4801.
[7] C.Z. Zhou, X.Q. Yang, G.H. Luan, J. Mater. Sci. 41 (2006) 2771–2777.
[8] Y.S. Sato, F. Yamashita, Y. Sugiura, S.H.C. Park, H. Kokawa, Scr. Mater. 50 (2004) 365–369.
[9] S.S. Di, X.Q. Yang, G.H. Luan, B. Jian, Mater. Sci. Eng. A 435 (2006) 389–395.
[10] S.M. Xu, X.M. Deng, Acta Mater. 56 (2008) 1326–1341.
[11] S.R. Ren, Z.Y. Ma, L.Q. Chen, Mater. Sci. Eng. A 479 (2008) 293–299.
[12] Y.S. Sato, H. Takauchi, S.H.C. Park, H. Kokawa, Mater. Sci. Eng. A 405 (2005) 333–338.
[13] Z.M. Yin, Q.L. Pan, Y.H. Zhang, F. Jiang, Mater. Sci. Eng. A 280 (2000) 151–155.
[14] M.J. Jones, F.J. Humphreys, Acta Mater. 51 (2003) 2149–2159.
[15] E.A. Marquis, D.N. Seidman, Acta Mater. 53 (2005) 4259–4268.
[16] X. Sauvage, A. Dede, A.C. Munoz, B. Huneau, Mater. Sci. Eng. A 491 (2008) 364–371.
[17] T.G. Nieh, R. Kaibyshev, L.M. Hsiung, N. Nguyen, J. Wadsworth, Scr. Mater. 36 (1997) 1011–1016.
[18] J. Zhao, F. Jiang, H.G. Jian, K. Wen, L. Jiang, X.B. Chen, Mater. Des. 31 (2010) 306–311.
[19] A.C. Munoz, G. Rueckert, B. Huneau, X. Sauvage, S. Marya, J. Mater. Process. Technol. 197 (2008) 337–343.
[20] Y.S. Sato, H. Kokawa, M. Enomoto, S. Jogan, Metall. Mater. Trans. A 30 (1999) 2429–2437.
[21] F.C. Liu, Z.Y. Ma, Acta Metall. Sin. 44 (2008) 319–324.
[22] A.A.M. da Silva, E. Arruti, G. Janeiro, E. Aldanondo, P. Alvarez, A. Echeverria, Mater. Des. 32 (2011) 2021–2027.
[23] S. Lim, S. Kim, C.G. Lee, C.D. Yim, S.J. Kim, Metall. Mater. Trans. A 36 (2005) 1609–1612.
[24] N. Afrin, D.L. Chen, X. Cao, M. Jahazi, Mater. Sci. Eng. A 472 (2008) 179–186.
[25] H.J. Liu, H. Fujii, M. Maeda, K. Nogi, J. Mater. Process. Technol. 142 (2003) 692–696.
[26] Y.S. Sato, H. Kokawa, Metall. Mater. Trans. A 32 (2001) 3023–3031.
[27] S. Mironov, Y. Motohashi, T. Ito, A. Goloborodko, K. Funarni, R. Kaibyshev, Mater. Trans. 48 (2007) 3140–3148.